Available online at www.sciencedirect.com

jmr&t Journal of Materials Research and Technology

journal homepage: www.elsevier.com/locate/jmrt

Original Article

Wire and arc additive manufacturing of 316L stainless steel/Inconel 625 functionally graded material: development and characterization

Tiago A. Rodrigues [a,*], *Francisco Werley Cipriano Farias* [a], *Kaiping Zhang* [b], *A. Shamsolhodaei* [b], *Jiajia Shen* [a], *N. Zhou* [b], *Norbert Schell* [c], *Jan Capek* [d], *E. Polatidis* [d], *Telmo G. Santos* [a], *J.P. Oliveira* [a,e,**]

[a] *UNIDEMI, Department of Mechanical and Industrial Engineering, NOVA School of Science and Technology, Universidade NOVA de Lisboa, 2829-516, Caparica, Portugal*

[b] *Centre of Advanced Materials Joining, Department of Mechanical & Mechatronics Engineering, University of Waterloo, 200 University Avenue West, Waterloo, Ontario, N2L 3G1, Canada*

[c] *Helmholtz-Zentrum Hereon, Institute of Materials Physics, Max-Planck-Str. 1, 21502, Geesthacht, Germany*

[d] *Paul Scherrer Institute, Laboratory for Neutron Scattering and Imaging (LNS), 5232, Villigen PSI, Switzerland*

[e] *CENIMAT|i3N, Department of Materials Science, School of Science and Technology, NOVA University Lisbon, Caparica, Portugal*

ARTICLE INFO

Article history:
Received 11 July 2022
Accepted 30 August 2022
Available online 6 September 2022

Keywords:
Wire and arc additive manufacturing (WAAM)
Functionally graded material (FGM)
Stainless steel 316
Inconel 625

ABSTRACT

In this work, a 316L stainless steel to Inconel 625 functionally graded material (FGM) was built using different deposition strategies (named as direct and smooth-type interfaces) by Twin-Wire and Arc Additive Manufacturing (T-WAAM). This combination of materials is of interest in chemical plants, oil & gas, and nuclear applications, where high corrosion and wear resistance are essential requirements. Although these properties are superior in Inconel 625, replacing Inconel with stainless steel in strategic regions of structural components can reduce the overall costs and parts' weight. Both direct and smooth transition interfaces were tested and characterized. Microscopic analysis revealed that each interface and the as-built samples had an austenitic matrix, and every sample was well bonded and free of defects. Different types of microstructures evolved at the interfaces due to distinct gradients in composition. Synchrotron X-ray diffraction measurements showed that the smooth-gradient produced secondary phases, such as δ-phase (Ni_3Nb) and carbides, that were not present with the direct interface strategy. Overall, the properties were superior in the FGM with a direct interface, which experienced higher strengths and elongations upon failure. Moreover, neutron diffraction measurements revealed that lower residual stresses developed in the direct interface FGM than in the smooth gradient FGM.

* Corresponding author.
** Corresponding author.
E-mail addresses: tma.rodrigues@campus.fct.unl.pt (T.A. Rodrigues), jp.oliveira@fct.unl.pt (J.P. Oliveira).

https://doi.org/10.1016/j.jmrt.2022.08.169

1. Introduction

The concept of Functionally Graded Materials (FGMs) was proposed in an attempt to develop high-performance heat-resistant materials, in which heat-resistant ceramics were blended with metals [1]. FGMs are an advanced class of heterogeneous materials that exhibit a controlled spatial variation of their composition and properties, leading to gradual changes in their performance (thermal/electric conductivity, corrosion resistance, mechanical, biochemical, and so on). The main idea behind FGMs consists of a material that cannot deliver all design requirements and a different material suitable for specific locations and operational conditions. Due to this synergic effect, FGMs can be applied in different fields, e.g., biomedical, automotive and aerospace, electronics, optics, nuclear applications, reactor components, and energy conversion [2]. FGMs can be characterized either by a gradual or a discontinuous/abrupt transition between materials. For abrupt transitions (direct interface), parts can experience significant stresses and chemical incompatibility. In contrast, a continuous/gradual transition could minimize these issues, and improve the mechanical properties at the interface [3,4].

Arc-based Directed Energy Deposition (DED-arc), commonly called Wire and Arc Additive Manufacturing (WAAM), is a valuable manufacturing technique for the fabrication of FGMs. Its production can be easily employed with a machine equipped with multiple and independent wire feeders, which allows the creation of parts with gradients of composition and properties in multiple directions. Using two wires simultaneously is designated as Twin-Wire and Arc Additive Manufacturing (T-WAAM). Nonetheless, combining two materials in the same molten pool brings forth perplexing challenges, including the potential formation of undesirable intermetallic compounds, which can reduce the weldability/printability (e.g., due to the formation of hot cracks and high hardness regions) and induce premature failure [2]. Moreover, mismatches in the thermal expansion coefficients, differences in the melting temperature, and lack of solubility can cause cracking and embrittlement [5]. The different thermophysical properties of each wire can also imply significant disparities in the process parameters needed to ensure defect-free parts.

FGMs of 316L stainless steel to Inconel 625 are used in chemical plants, oil and gas, and nuclear industry applications. Especially in cladded pipes and valves where parts are inserted in two different environments, which require different corrosion and wear resistances (inner contact to corrosive fluids, e.g., crude oil with high CO_2 and H_2S content, and outside contact with the atmosphere [6–8]). Although these properties are superior in Inconel 625, replacing Inconel with stainless steel in strategic regions of structural parts can reduce the associated component costs. Both alloys exhibit as a matrix a single face-centered cubic (FCC) phase (γ), and their principal alloying elements are Fe, Cr, and Ni. Depending on the process and building strategy, some problems can occur, where hot cracks are especially prevalent.

Shah et al. [9], using laser-directed energy deposition (L-DED), analyzed the influence of the process parameters on the fabrication of a 316 stainless steel to Inconel 718 FGM. The authors demonstrated no evidence of cracks induced by thermal stresses, regardless of the parameters used. Since the susceptibility for liquation cracking increases with grain size [10], the fine microstructure of the bimetallic structure protects against this type of defect. X-ray diffraction detected Niobium carbides (NbC) and Laves (Fe_2Nb) at the interface. Chen et al. [11] studied a direct interface deposition of Inconel 625 on top of 316 stainless steel (type I-interface) and stainless steel 316 on top of Inconel 625 layers (type II-interface). The authors found that the type I interface is more favorable since a gradual compositional transition can be obtained due to the lower density and viscosity of stainless steel compared to Inconel 625, which aids in promoting a good mixing of the two materials. In the type II interface, the higher density and higher viscosity of Inconel hindered the compositional mixing and thus generated a compositional sudden-change zone, causing cracks in the type II interface. Through laser DED, Carrol et al. [12] fabricated an FGM of 304L stainless steel to Inconel 625 with 24 layers as the transition region, where the composition was changed in 4 vol.% steps. Large cracks (>200 μm) were found in approximately 79 wt. % stainless steel and 21 wt.% Inconel 625. Further characterization and thermodynamic calculations allowed the authors to confirm that cracks were promoted by the formation of Nb- and Mo-based eutectics, which have a large stability region between 500 °C and 1045 °C.

Despite the direct transition zone (absence of gradually mixed filler metal) commonly observed in stainless steel (used as base metal) arc-welded with Inconel 625 (used as filler metal), the WAAM literature on 316L stainless steel to Inconel 625 FGMs is still scarce and divergent. Thus, the present work attempts to optimize and compare the FGM's properties built with different deposition strategies. Moreover, it will be demonstrated that with WAAM, a completely smooth transition can be obtained without defects, which is yet to be obtained with other fusion-based additive manufacturing processes.

2. Materials and methods

2.1. *Experimental setup*

The 316L stainless steel to Inconel 625 functionally graded materials were made using AWS A5.9 ER 316LSi (316L stainless steel) and AWS ERNiCrMo-3 (Inconel 625) welding wires, both 1 mm in diameter, whose composition can be found in Table 1. A gas tungsten arc welding (GTAW) Great Tool Spitfire TIG DC 1700 HF power source was used. This power source has a high-frequency start, enabling the electric arc to start without needing contact between the non-consumable tungsten electrode and the substrate. An in-house multiple-wire feed system, presented in a previous work conducted by the authors of the present paper, was used for these experiments [13]. The fabricated parts were single walls, 130 mm in length, and the current was set at 65 A for every layer of each material. A mild steel plate ($180 \times 50 \times 6$ mm^3) was used as the substrate.

Preliminary parameter selection enabled suitable process parameters (refer to Table 2) that resulted in a similar height and width for both materials. These parameters were used to

Table 1 – Chemical composition of the wire feedstocks used in this work (wt.%).

Alloy	C	Mn	Si	Nb	Ti	Al	Ni	Cr	Mo	Cu	Fe
316L Stainless steel (ER 316LSi)	0.03	1.60	0.65	–	–	–	11	18.5	2.50	0.75	Bal.
Inconel 625 (ER NiCrMo-3)	0.1	0.5	0.5	3.5	0.4	0.4	Bal.	21.5	9	0.5	5

fabricate the following samples: (i) 40-layer samples of 316L stainless steel (Fig. 1a), (ii) 40-layer samples of Inconel 625 (Fig. 1b), (iii) direct interface of 20 layers of 316L stainless steel to 20 layers of Inconel 625 (FGM 100-100; Fig. 1c), and (iv) smooth transition FGM (FGM 5; Fig. 1d), i.e., 15 layers of 316L stainless steel, 19 layers mixing the filler wires made in steps of 5 wt.% at each layer, and 15 layers of Inconel 625. Samples (i) and (ii) were used to benchmark 316L stainless steel and Inconel 625, respectively.

2.2. Characterization methods

Cross-sections were cut, polished, and then etched from each sample. Before microscopic observations, samples were polished using abrasive papers with grits from P80 to P2000 and polished using a 1 μm diamond suspension. All samples were electrolytically etched in 10 wt.% chromium trioxide (Cr_2O_3) dissolved in distilled water at a potential of 5 V for 20 s. Microstructural examinations were carried out using a SU3800 Hitachi scanning electron microscope (SEM) and a Zeiss FESEM 1530 scanning electron microscope (SEM) equipped with an Energy Dispersive X-Ray Spectroscopy (EDS) system.

ThermoCalc was used with the TCFE11 thermodynamic database to assess the phases that would form during solidification (Scheil-Gulliver model). The Scheil-Gulliver model assumes equilibrium at the solid/liquid interface, complete diffusion in the liquid, negligible diffusion in the solid, fast diffusion of carbon and nitrogen (interstitial elements), and negligible dendrite tip undercooling.

Synchrotron X-ray diffraction measurements were performed at the High Energy Materials Science beamline at PETRA III, DESY, Hamburg, Germany, with a beam energy of 87.1 keV ($\lambda = 0.14235$ Å). A 2D PerkinElmer detector with a pixel size of 200 μm was used to capture the Debye–Scherrer diffraction rings. The Fit2D [14] software (freely available) was used to integrate along the whole azimuthal angle (φ) the raw diffraction data to obtain conventional (Intensity vs. d-spacing) diffractograms. For the X-ray diffraction experiments, a beam size of 1 × 1 mm was used with an exposure time of 5 s. Besides, the detector and beamline optics parameters were calibrated with LaB_6 calibrant powder.

Table 2 – Process parameters used to fabricate the 316L stainless steel/Inconel 625 FGM.

Process	Gas tungsten arc welding (GTAW)
Travel speed	120 mm/min
Wire feed speed	1 m/min
Average current	65 A
Shielding gas	Argon 99.99%
Shielding gas flow rate	16 L/min

Residual stresses were measured in FGM 100-100 and FGM 5 samples using neutron diffraction. These measurements were made on the POLDI instrument at the Swiss Spallation Neutron Source, SINQ, at the Paul Scherrer Institute, Switzerland. A cubic gauge volume of 3.8 × 3.8 × 3.8 mm^3 was defined by a pair of diaphragms in the incident beam and a radial collimator on the diffracted beam. The data were fitted using a Gaussian function and the Pawley fit method implemented in Mantid [15]. Strains were measured in the samples' longitudinal, normal, and transverse directions.

Since every change in the lattice parameter of the material usually indicates changes in the material strains, equation (1) was used to measure the principal strains (ε), where i denotates each direction (x, y, z), and a and a_0, correspond to the strained and unstrained lattice parameters, respectively.

$$\varepsilon_{ii} = \frac{a_i - a_{0,i}}{a_{0,i}} \quad (1)$$

Finally, the principal stresses were calculated using the triaxial form of the Hooke's Law equation (2), where E [Pa] is the elastic modulus, and ν [-] is the Poisson's ratio.

$$\sigma_{ii} = \frac{E}{(1+\upsilon)(1-2\upsilon)}\left[(1-\upsilon)\varepsilon_{ii} + \upsilon\left(\varepsilon_{jj} + \varepsilon_{kk}\right)\right] \quad (2)$$

Young's modulus and Poisson's ratio values are required for each compositional ratio. Thus, it was used 193 GPa as $E_{SS\ 316L}$ and 0.27 as $\upsilon_{SS\ 316L}$ when the amount of stainless steel was higher in the FGM, and 208 GPa as E_{Inc625} and 0.27 υ_{Inc625} were used when the amount of Inconel was higher. Although these constants could be slightly different in the intermediate regions, when both materials are mixed, such considerations would result in marginal differences. Two lattice constant (a_0), one for the stainless steel and the other for the Inconel regions, of the stress-free condition were measured by synchrotron x-ray diffraction on as-built samples heat-treated at 1050 °C for 2 h following slow air cooling.

Microhardness testing was performed with a Mitutoyo HM-112 Hardness Testing Machine. Measurements were performed in a straight line from the substrate to the last deposited layer of each sample, distancing 250 μm between indentations with a load of 4.9 N. A four-point potential drop technique previously described by Sorger et al. [16] was used to measure the changes in electrical conductivity between samples. Measurements were made across the full height, with a needle spacing of 635 μm and an imposed current of 80 mA. Uniaxial tensile tests were performed on an MTS servo-hydraulic press with a capacity of 100 kN and with a displacement rate of 1 mm/min. Specimens were prepared so that the transition between materials was exactly at the middle of the tensile specimens. Digital Image Correlation (DIC) during tensile testing was performed using Ncorr 2D digital image correlation MATLAB software toolbox [17].

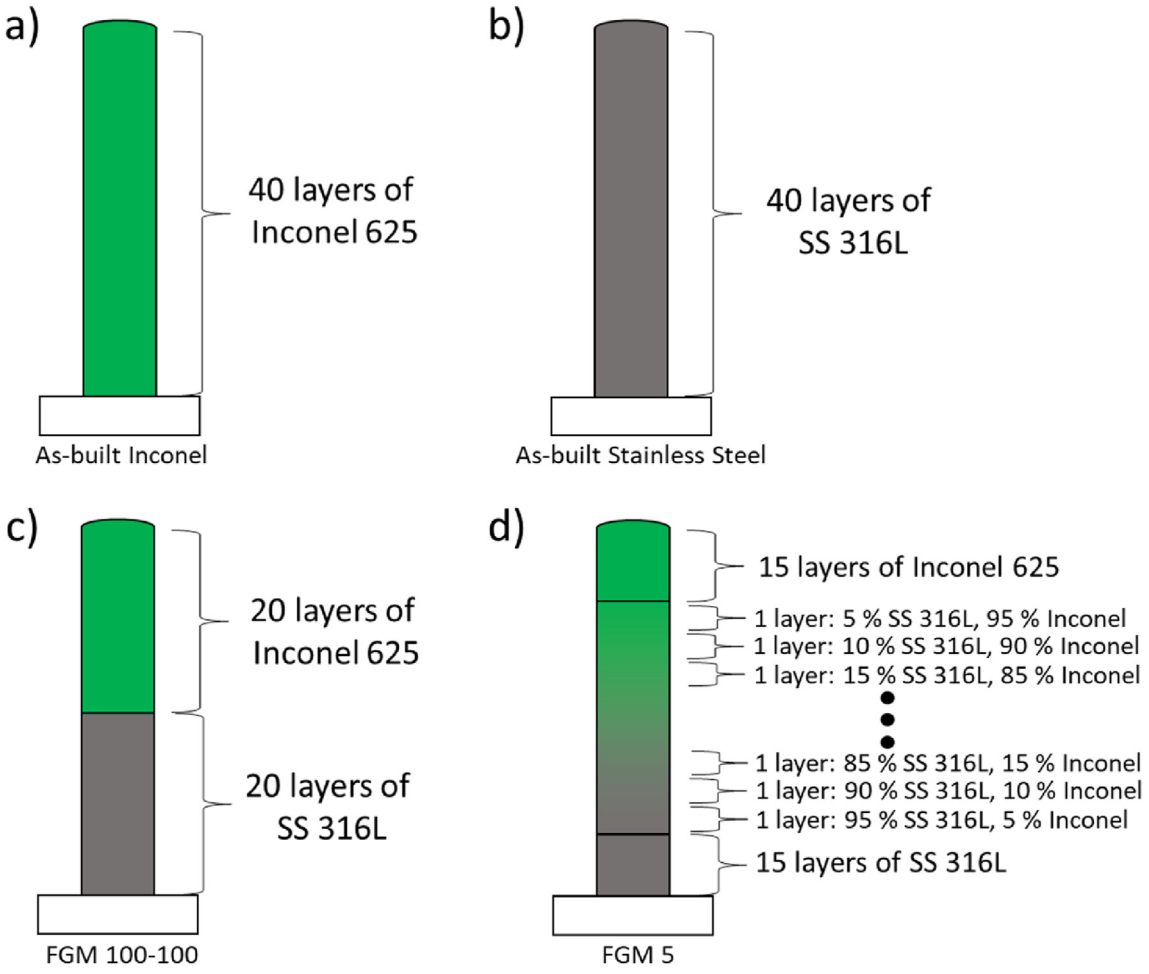

Fig. 1 – Build strategies employed to fabricate different FGMs: a) and b) as-built control samples of Inconel 625 and 316L stainless steel, respectively; c) Direct interface from stainless steel to Inconel (FGM 100-100); d) Smooth transition by varying the percentage of filler material within each layer in concentration steps of 5 wt. % (FGM 5).

3. Results and discussion

3.1. *Microscopic characterization*

Macroscopic and higher magnification SEM images were taken at different regions of each FGM and are depicted in Figs. 2 and 3 for the FGM 100-100 and FGM 5, respectively. Each multi-layer FGM showed good bonding between layers, with a columnar dendritic growth almost parallel to the building direction, mainly determined by the direction of heat extraction. Despite the different compositional ratios tested in each sample, no evidence of cracks induced by the thermal stresses associated with the WAAM process was observed in the different transversal and longitudinal cuts made and during face milling of the parts to build tensile testing samples.

In the top layers of the FGM build with a direct interface, Fig. 2(b and c), the microstructure is mainly composed of a Ni-FCC matrix that is solidified in a columnar-dendritic mode. In the bottom regions corresponding to the stainless-steel region (Fig. 2e), the bright regions correspond to austenite (γ) while the dark areas are retained δ-ferrite. The stainless steel feedstock wire in this work has a Cr_{eq}/Ni_{eq} ratio of 1.69, which considering the WRC-1992 constitution diagram corresponds to a ferritic-austenitic (FA) solidification mode (Liquid→Liquid + δ→Liquid + δ + γ→δ + γ) [18]. In the mixture region (Fig. 2d), the microstructure is of columnar and equiaxed dendritic type with segregants embedded in the interdendritic regions, as marked by red arrows. The changes in the microstructure depicted in Fig. 2d) in comparison with Fig. 2c) are due to the complex cyclic thermal history during deposition which resulted in elemental migration at the interface. According to Silva et al. [19], the increase in the Fe content (transition zone; interface) enhances the interdendritic segregation of Mo and Nb (reducing the partition coefficient), which favors the formation of Laves phase in the interdendritic regions (eutectic transformation) corroborating the observed results. Due to the participation of Ni, the solidification mode was altered from FA to A and no evidence of δ-ferrite was observed at the interface. It is worth noting that the Laves phase content should be minimized since it can reduce the material ductility and corrosion resistance [4,20].

The microstructure of the FGM made in compositional steps of 5 wt. % is detailed in Fig. 3. It can be perceived a

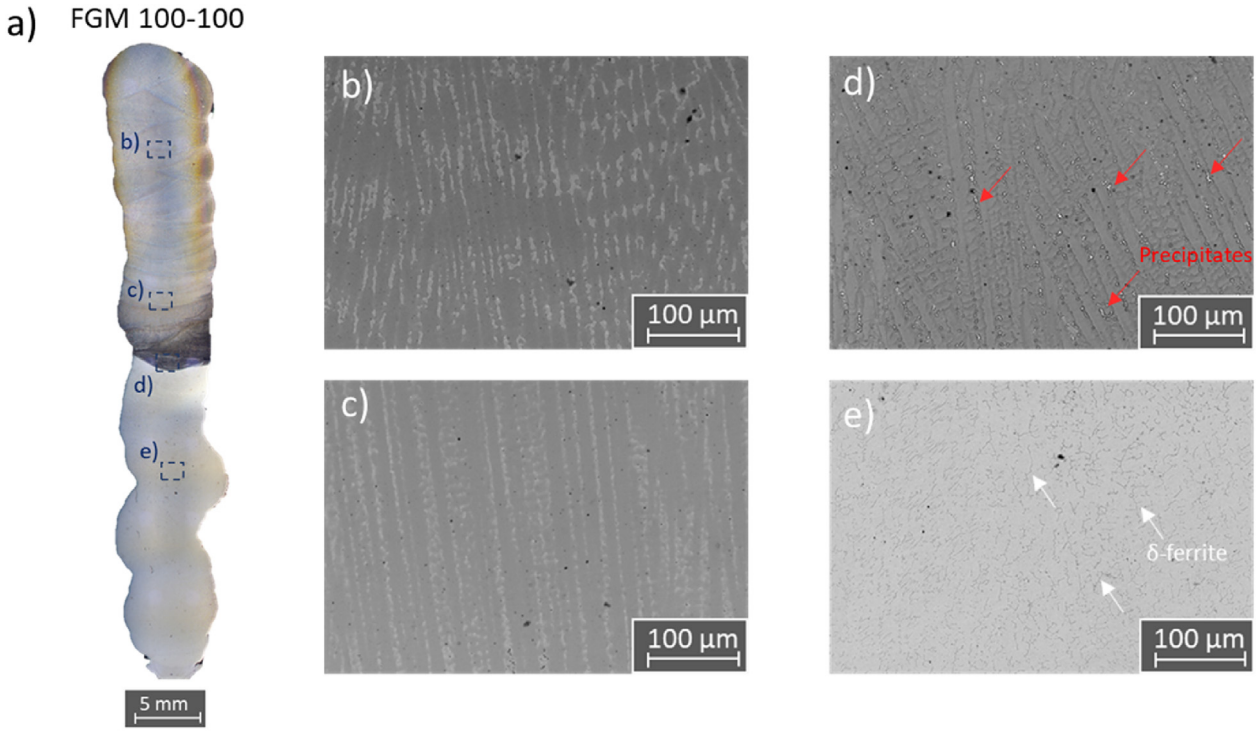

Fig. 2 – (a) Cross-section overview of the direct interface FGM part; Detail of the region with: (b) and (c) 100% Inconel 625, (d) interfacial region, and (e) 100% 316L Stainless steel.

gradient of microstructures without sudden/abrupt changes. In the range of 0–15 wt. % of stainless steel (Fig. 3b–d), the microstructure resembles that of as-built Inconel 625, which presents dendrites (white features) aligned with the build direction in a γ-matrix. From 35 to 55 wt.% of stainless steel, the microstructure contains dendrites with some precipitates inside both primary and secondary arms. When the stainless-steel composition increases to 75 wt.%, still no δ-ferrite was

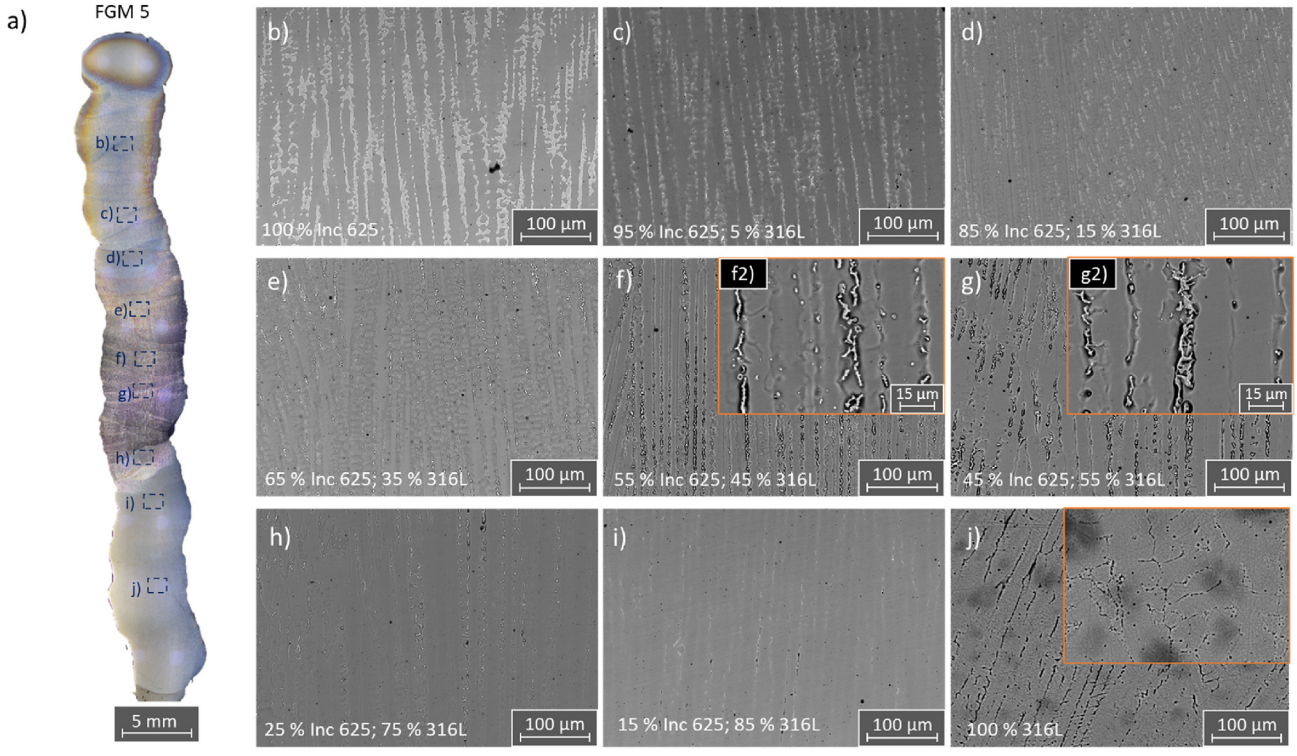

Fig. 3 – Microstructure of the FGM made in weight percentage steps of 5% (FGM 5).

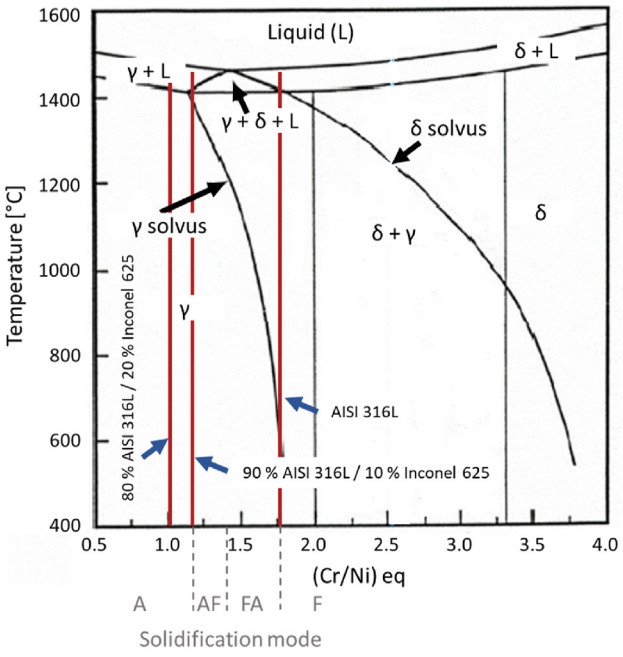

Fig. 4 – Pseudo-binary FeCrNi diagram at 70% Fe (adapted from [21]).

found, but it is visible the presence of other precipitates. Regions with more than 85 wt.% of stainless steel presented δ-ferrite dendrites as dark regions in an austenite matrix. The precipitates at different locations of the FGM will be further discussed, considering the synchrotron X-ray diffraction analysis performed at the same locations. From the pseudo-binary diagram of stainless steel with 70 wt.% Fe (Fig. 4), it can be perceived that below a weight percentage of 90% of 316L stainless steel, assuming a homogeneous composition, the FGM microstructure is expected to be depleted of δ-ferrite.

3.2. *Synchrotron X-ray diffraction*

The synchrotron X-ray diffraction measurements performed in the FGM 100-100 sample are presented in Fig. 5. The material displayed FCC austenite (γ) as the primary phase, but both base materials had different secondary phases. The Inconel 625 regions presented γ′, γ″, MC carbides, and Laves phase, while the stainless steel has both δ-ferrite and σ phase. In the middle region, where the two materials are mixed, no other phases were discernible besides those already identified in the base materials.

The synchrotron X-ray diffraction measurements (detailed in Fig. 6) in the FGM 5 (smooth-type interface) qualitative show that with the increase of Fe, new phases (δ-phase (Ni_3Nb), σ, and MC carbides) are formed between the regions with 60–80 wt. % of Inconel. This result is in accordance with Silva et al. [22], who found that an increase in the Fe content in Inconel 625 increases the fraction of δ-phase (Ni_3Nb) precipitates. Solidification of Inconel 625 is complex and largely dependent on the amount of each alloying element. Cieslak et al. [23] studied the influence of different elements on the solidification modes of Inconel 625 and verified that Nb significantly impacted the melting temperature range.

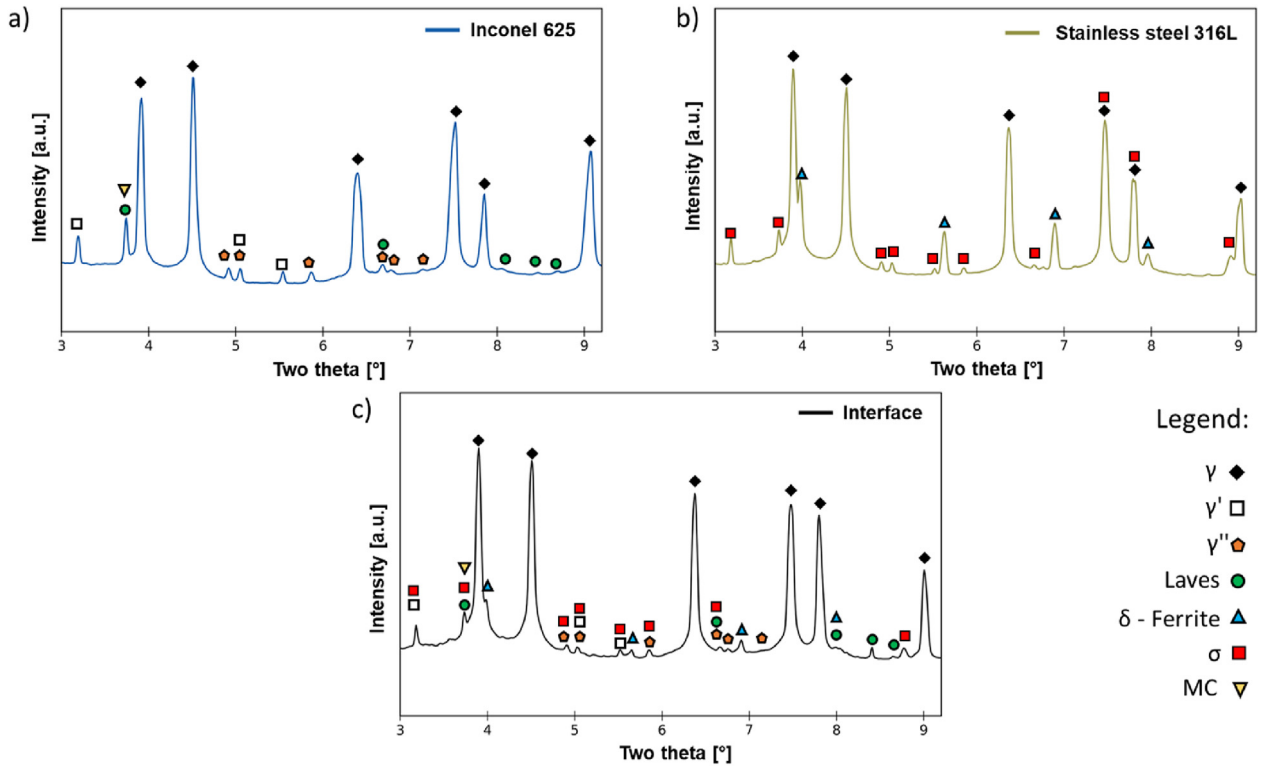

Fig. 5 – Synchrotron X-ray diffraction analysis performed in regions comprising: a) Inconel 625, b) 316L Stainless steel, c) Interface.

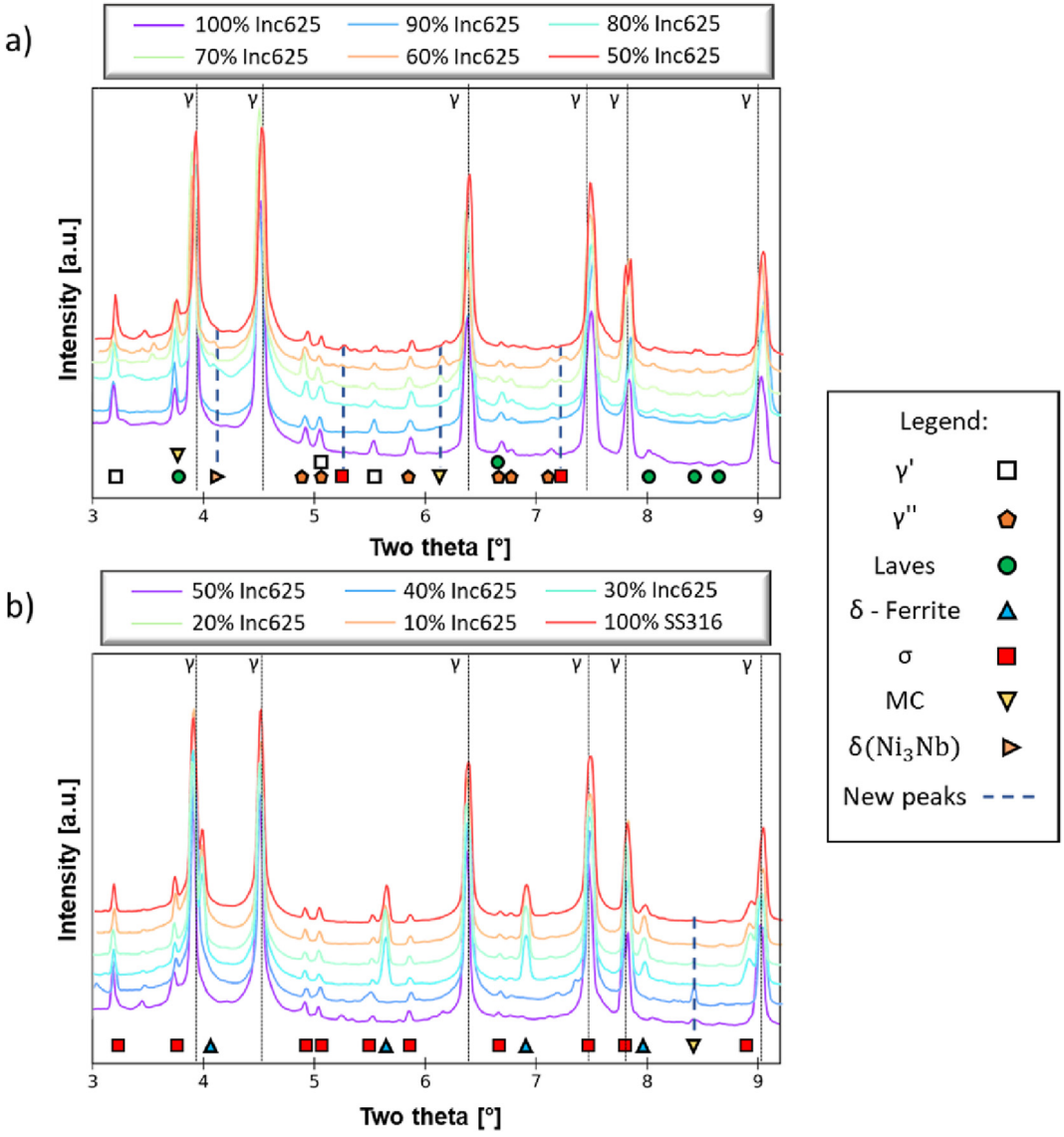

Fig. 6 – Synchrotron X-ray measurements taken from the substrate to the last deposited layer in FGM 5 sample.

Moreover, the solubility of Nb in the γ matrix is reduced with the increased presence of Cr, Mo, and Fe, which reduces its distribution coefficient and increases the amount of eutectic phases (especially carbides) in the interdendritic regions. The excess of Fe also favors the formation of topologically close-packed (TCP) phases, such as Laves phase during solidification with a stoichiometry rich in Fe, Fe_2Nb, or Fe_2Mo [23], and the precipitation of σ phase [24], as verified in Fig. 6a.

In the middle region with a weight percentage of 50 wt. % of each material, since the Inconel secondary phases (γ′, γ″ and Laves phase) diffract at the same angles as the σ-phase, it is impossible to characterize this region accurately. At 40 wt. % of Inconel, MC carbides were observed. In agreement with the optical micrographs in Fig. 3 and the phase diagram in Fig. 5, δ-ferrite is present when the amount of Inconel 625 is below 30%.

Thermodynamic calculations for a weight percentage of 85, 70, 60, and 50 wt.% of stainless steel were computed, and these are presented respectively in Fig. 7(a–d). For 85 wt.% of stainless steel, the solidification path predicts austenite formation, followed by M_6C, the first eutectic phase to form along the interdendritic boundaries. With further cooling, Laves phase forms. These thermodynamic calculations also confirm that the solidification mode changes for this composition onwards (<85 wt.%), and δ-ferrite does not form anymore.

When the weight percentage of stainless steel decreases to 70 and 60 wt.%, the Scheil-Gulliver calculations, besides the hexagonal Laves phase and M_6C carbides, also predict the precipitation of σ, $M_{23}C_6$, and δ-phase (Ni_3Nb). These results are corroborated by the synchrotron X-ray diffraction results, which indicated the presence of carbides and σ phase between the regions with 40 and 60 wt.% of stainless steel. From Fig. 7(a–c), an increase in the solidification range can be noticed, making the material more likely to experience solidification cracking as the different concentrations make the material more prone to segregation and precipitation of

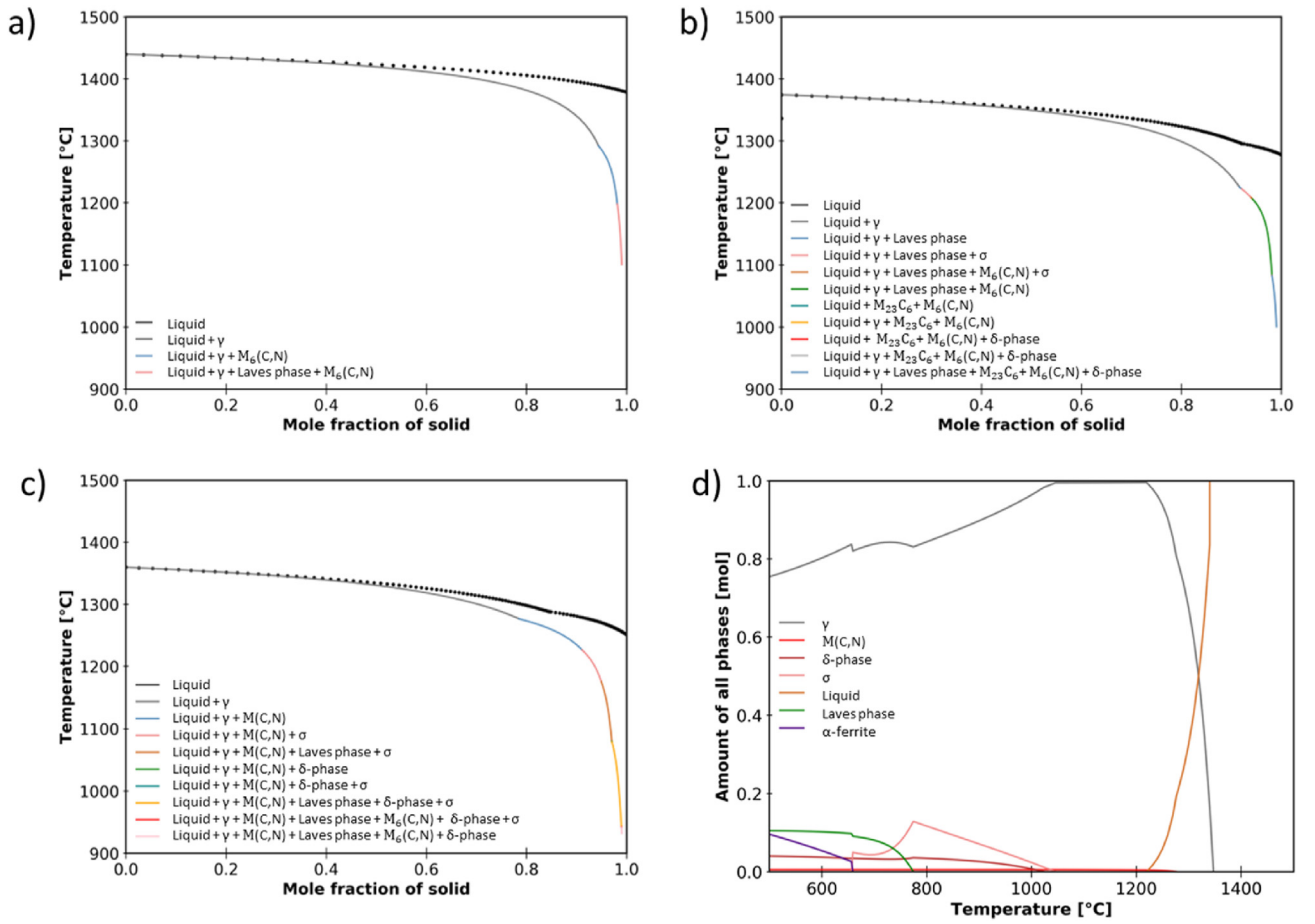

Fig. 7 – Scheil-Gulliver simulations for a stainless-steel wt. % of: a) 85%, b) 70% and c) 60%; d) Thermodynamic equilibrium calculations considering 50 wt.% of Inconel and 316L stainless steel.

secondary phases as Nb-rich Laves, which have a low melting point [25,26].

Fig. 6(d) shows the equilibrium phase diagram for a weight percentage of 50/50 wt. %. This diagram considers the hypothetical situation of an infinitely slow cooling in which the composition was allowed to reach an equilibrium condition at each temperature step. Austenite was the first to solidify from the liquid at around 1340 °C, followed by σ that started to form at 1045 °C, increasing in amount until 790 °C, and then suddenly dropped off at 656 °C. Following these occurrences, δ-phase (Ni_3Nb) was in equilibrium between 500 and 1023 °C in amounts up to 4 at.%. Laves began to precipitate at 770 °C and should represent around 10 at. %, while α-ferrite (BCC) began to precipitate at 656 °C, resultant of the direct transformation of σ→α-ferrite.

3.3. *Scanning electron microscopy with energy dispersive spectroscopy*

The distribution of elements on the cross-section of the FGM 100-100 part was investigated by SEM/EDS. As shown in Fig. 8, moving from the region of Inconel 625 to the stainless steel side, the Fe content increased, but Ni, Mo, and Nb contents decreased. The segregated regions in Inconel are enriched with Nb, indicating the presence of γ'' in these areas. In Fig. 8(a), it is observed that the interface between materials is sudden (absence of macrosegregation [27]) without any gradient and an evident transition of grain structure with negligible elemental diffusion.

Fig. 9 shows the distribution of elements across the precipitates found in the interdendritic regions of the FGM 5 sample around the compositional region with 50 wt.% stainless steel/50 wt.% Inconel 625. Severe segregation of Nb and Mo into these interdendritic spaces might indicate the presence of Laves phase (Cr_2Mo) and carbides (NbC).

3.4. *Residual stresses measurements*

Fig. 10 compares the residual stresses in the three orthogonal directions (x, y, z) measured along a central line across the FGM 100-100 and FGM 5 walls. The results show compressive stresses in the region where the two materials are mixed of FGM 100-100 with a magnitude up to 180 MPa in the building direction (Fig. 10a). In the other two directions, the magnitude was not higher than 80 MPa throughout the height of the sample. FGM 5 experienced considerably more residual stresses than FGM 100-100 (Fig. 10b). The neutron diffraction results depict tensile stresses at the interface, near a weight

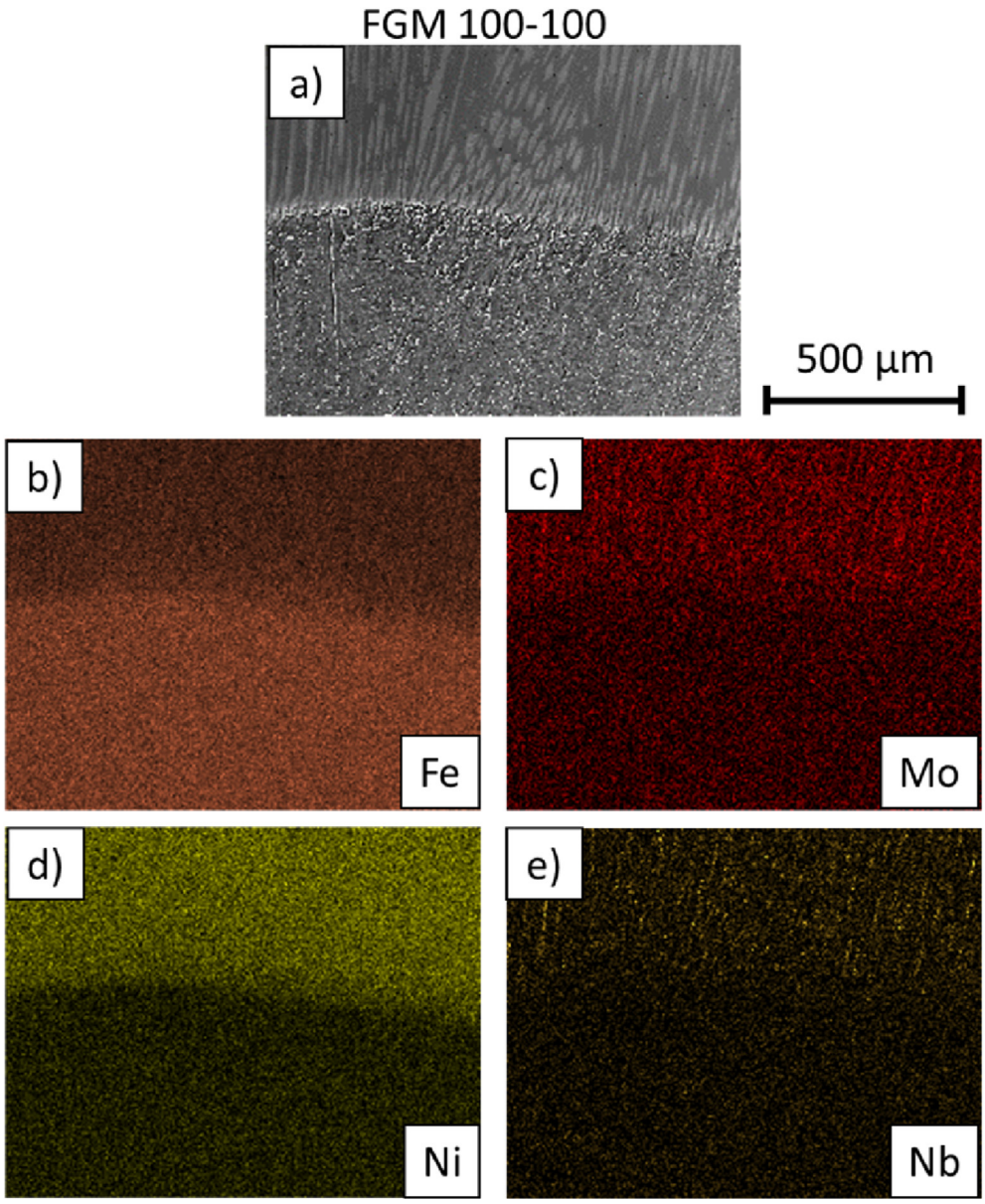

Fig. 8 – Scanning electron microscopy (SEM) and Energy-dispersive X-ray spectroscopy (EDS) mapping of the FGM 100-100 interface.

percentage of 55 wt.% Inconel, with magnitudes up to 314, 348, and 468 MPa in the x, y, and z directions, respectively. The residual stresses being higher in the FGM 5 might be attributed to the potential deleterious concentrations resulting in the precipitation of δ-phase (Ni_3Nb), σ phase, and carbides. The existence of multiple precipitates with different stoichiometries and properties might result in strong volume mismatches and significant stresses that the material must accommodate. These results go against the common assumptions that a smooth gradient might be desirable for reducing internal stresses [28]. Such graded structures can indeed be of interest to decrease residual stresses provided that no detrimental phases are formed.

3.5. *Mechanical properties*

Fig. 11 depicts the micro-hardness and electrical conductivity measurements made from the first to the last deposited layer.

Fig. 11(a) shows similar hardness and tendencies in both samples (FGM 5 and FGM 100-100). In the first layers, the hardness is approximately 200 HV. Then it decreases to around 173 HV at around 35–40% of the total height. From this point onwards, it increases almost linearly until reaching the region with only Inconel 625 (>80% total height) with a maximum hardness of 220 HV. The increased hardness in the first layers of both samples is attributed to the high carbon content in the substrate and to the faster cooling rates that the

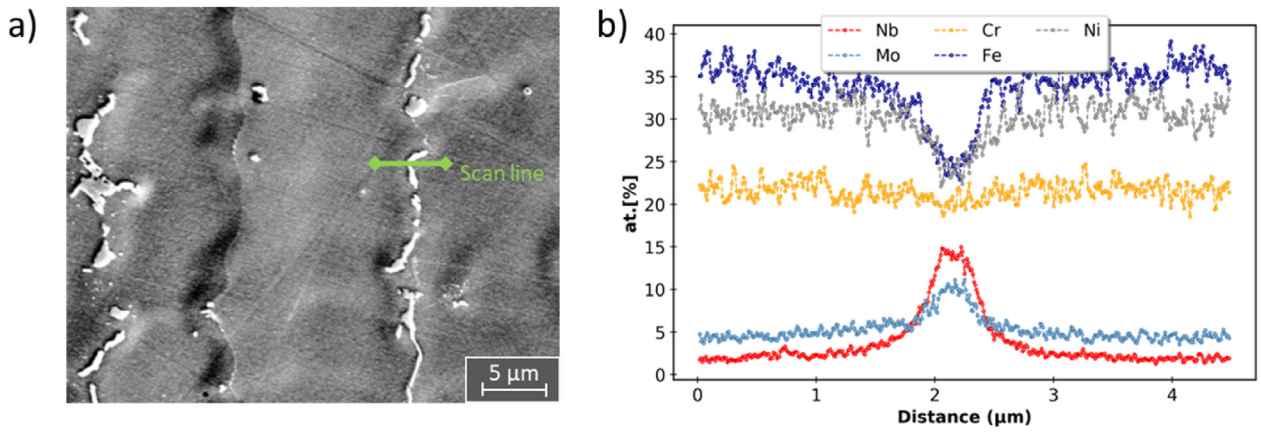

Fig. 9 – EDS line scan across the precipitates in the compositional region with 50 wt.% stainless steel/50 wt.% Inconel.

first layers undergo which results in a finer microstructure and less elemental segregation [29,30]. Only at around 18% of the parts' total height do the hardness values reach values similar to the average value of the as-built stainless steel 316 (≈183 HV). However, near the region between 35 and 40% of total height, the FGM 5 sample experiences a hardness decrease to 169 HV. This decrease is attributed to the decrease of the δ-ferrite content in the weight percentage of 70 wt.% stainless steel/30 wt.% Inconel in the FGM 5, since δ-ferrite is known to provide increased hardness in stainless steel [31]. This depletion of ferrite is explained by the increased content of Ni content in steel that shifts the Cr_{eq}/Ni_{eq} ratio to the left in the pseudo-binary diagram (refer to Fig. 4) changing the solidification mode. It is perceived that the as-built AISI 316 stainless steel composition solidification starts with δ-ferrite from the liquid (Liquid → Liquid + δ), which due to inter-dendritic segregation induces the formation of austenite, resulting in a ferritic-austenitic solidification (FA) mode (Liquid → Liquid + δ →Liquid + δ + γ → δ + γ). However, below an 80 wt.% of stainless steel, the solidification mode changes to mode A – single phase austenite (Liquid → Liquid + γ → γ), depleting δ-ferrite formation, which decreased the material's

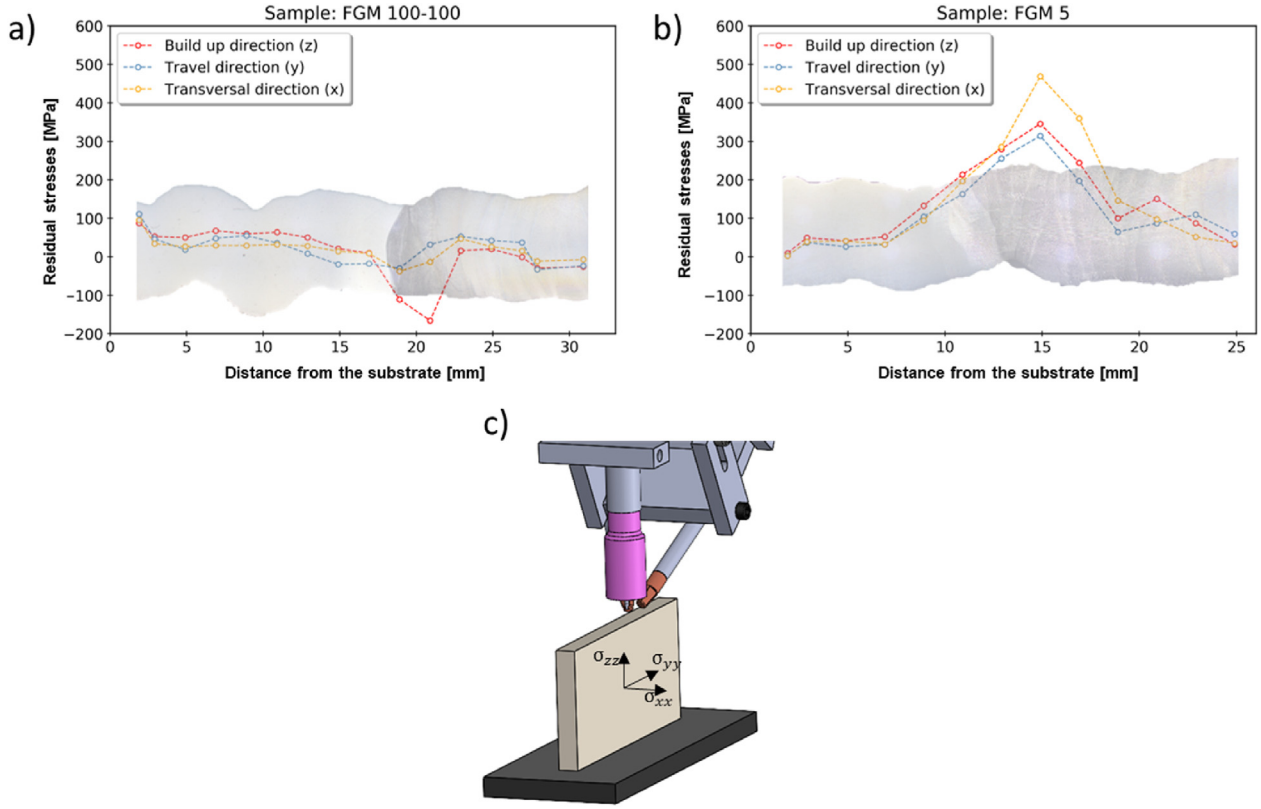

Fig. 10 – Residual stresses in the three principal directions (c) of the sample: a) FGM 100-100 (direct interface); b) FGM 5 (smooth transition).

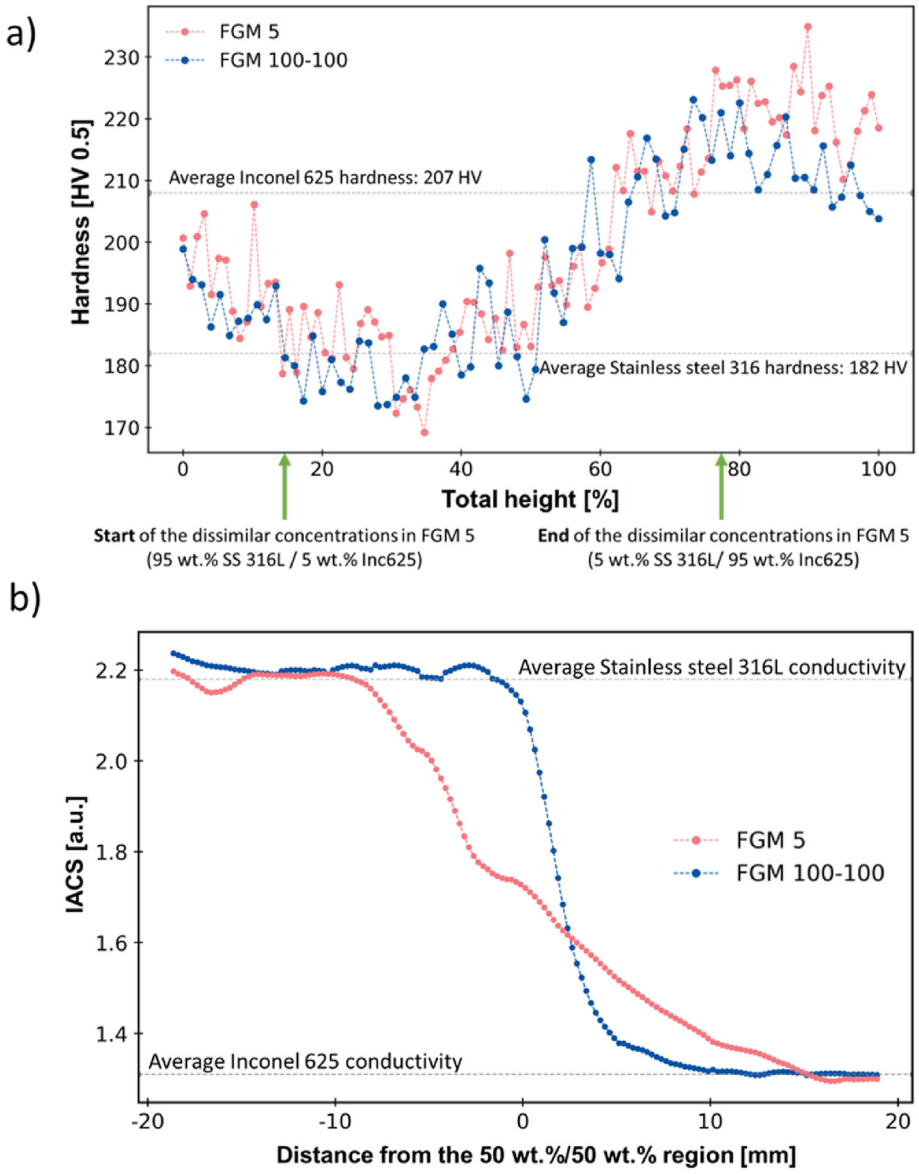

Fig. 11 – a) Comparison of hardness measurements between the two FGM fabricated (FGM 5 vs. FGM 100-100); b) Electrical conductivity measurements made starting in the first layer and ending on the last deposited one.

hardness. Such similarities were found in AISI 904L super-austenitic stainless steel welded joints, which had higher Ni, Cr, and Mo contents (solidification mode A, i.e., absence of δ-ferrite) than the AISI 316L stainless steel [32]. Moreover, the AISI 904L superaustenitic stainless steel welded joints had comparable hardness (172 HV) with the FGM's minimum (169 HV), due to the matching microstructure (only austenite). In addition, similarly to the AISI 904L superaustenitic stainless steel the increase in alloying elements (solid solution strengthening) does not translate into higher hardness in the AISI 316L stainless steel since the microstructure (austenite + δ-ferrite, and phase boundary effects) has a stronger effect than the solid solution strengthening effect. Kim et al. [33] also reported that the gradual chemical composition induces a soft region (≈170 HV) in an FGM (70 wt.% Inconel 718/30 wt.% stainless steel 316) fabricated by laser-DED, which also relates to the microstructure changes (absence of δ-ferrite), further corroborating the present discussion. As the Inconel 625 content increases with height (region with 50 wt.% = 50% total height), more Nb and Mo are added to the molten pool, allowing more secondary precipitates to form, which increases the material's hardness. Despite MC carbides and δ-phase (Ni_3Nb) being identified in the interface of the FGM 5 sample by synchrotron X-ray diffraction, the hardness measurements were identical between samples.

The electrical conductivity measurements are presented in Fig. 11(b). In the stainless-steel region, the electrical conductivity is, on average, 2.19% IACS and gradually decreases in each sample to approximately 1.31% IACS in the region that is only composed of Inconel 625. In the FGM 100-100, the dissolution of elements in the interface created a gradient region up

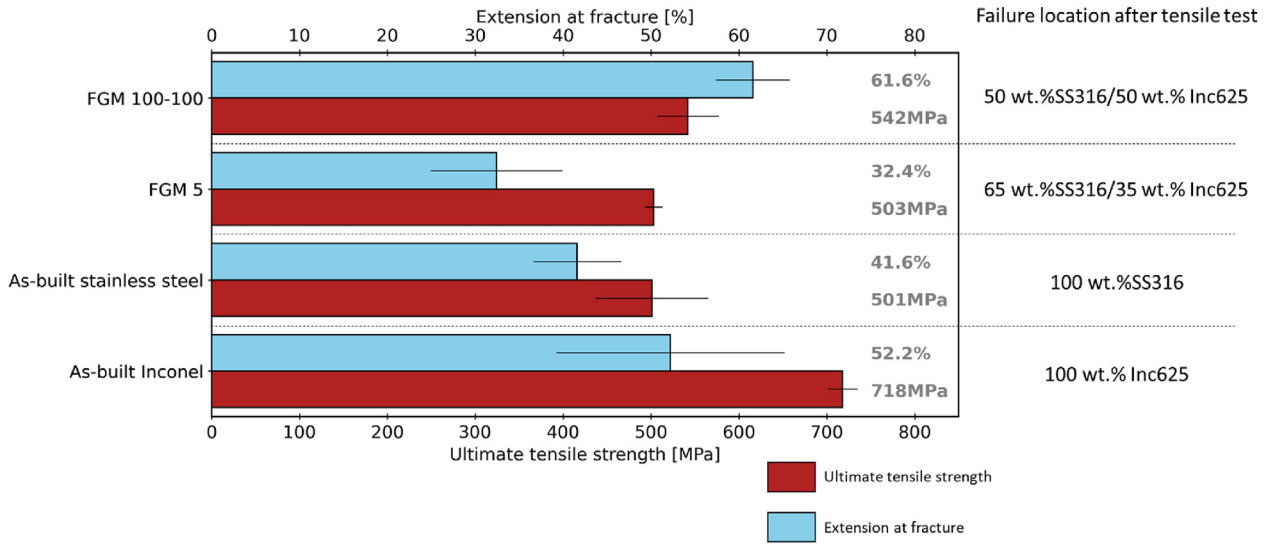

Fig. 12 – Average mechanical properties obtained from tensile testing from each WAAM fabricated condition and respective fracture location.

to 12 mm, corresponding to approximately 9 layers in length. These results also indicate the successful fabrication of a gradient material using a direct interface deposition strategy.

Specimens for tensile testing with the load direction aligned with the build-up direction (z-axis) were made to evaluate the properties with different depositions strategies. A summary of the average mechanical properties of the fabricated material, namely the ultimate tensile strength (UTS) and extension at fracture, is presented in Fig. 12. It can be perceived that the FGM 100-100 parts had an overall better behavior than the FGM 5 ones. The FGM 100-100 parts had an average UTS of 542 MPa and an elongation at fracture of 61.6%. The obtained UTS values are within the range of the as-built control samples (501 and 718 MPa, for stainless steel and Inconel, respectively). FGM 5 had UTS and extension at fracture values of 503 MPa and 32.4%, respectively. These values are similar to those found in the as-built control stainless steel 316L samples (501 MPa and 41.6%), which was expected since the fracture of the FGM 5 sample occurred near the region with 65 wt.% of stainless steel. The decrease in the extension at fracture can be attributed to the increase of interdendritic phases (both σ-phase and carbides) in comparison to the control sample (316L stainless steel) at the region where the fracture occurred (65 wt.% stainless steel), i.e., the mixing of the two metals induced a deleterious microstructure which causes a smaller ductility in comparison with the FGM 100-100 whose fracture occurred right at the middle of the specimens (50 wt.% stainless steel/50 wt.% Inconel 625). Similar behavior was found in the literature where a larger gradient between materials resulted in lower tensile strength and elongation at fracture. The existence of more layers with various mixing ratios made the material more prone to the existence of precipitates and inclusions [34].

During uniaxial tensile testing, the deformation distribution along the load direction (z) was evaluated at different zones of the joining interfaces using digital image correlation

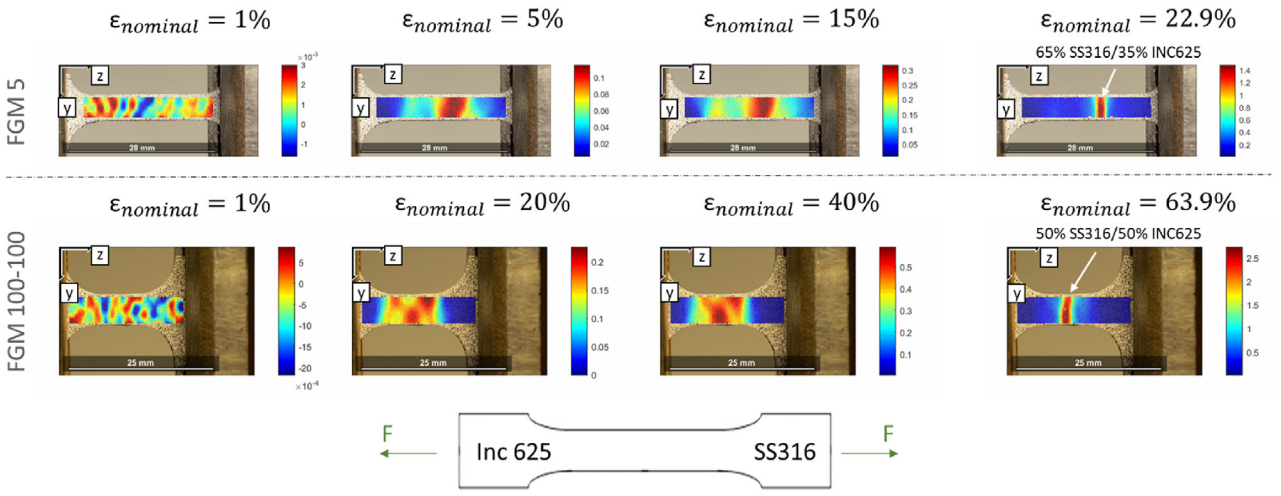

Fig. 13 – Strain measurements along the x-axis distribution during tensile testing of the FGM 5 and FGM 100-100.

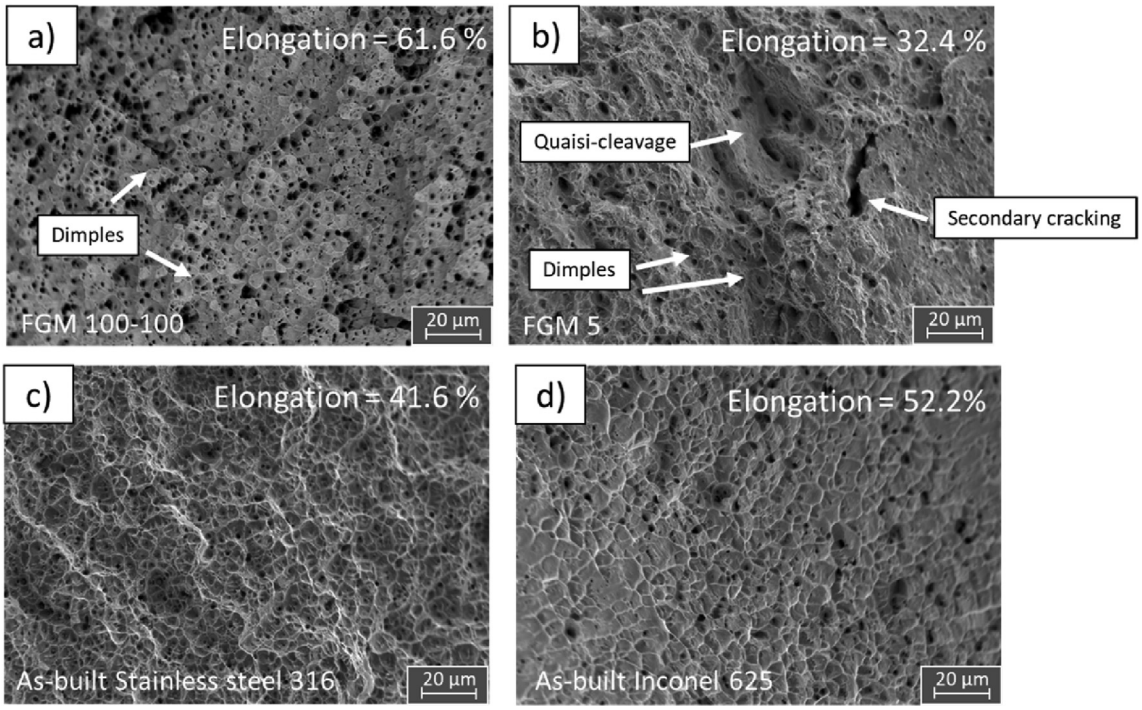

Fig. 14 – SEM images of the fracture surface of samples: (a) FGM 100-100; (b) FGM 5; (c) As-built 316 stainless steel; (d) As-built Inconel 625.

(DIC). The elongation stages for different nominal elongations are given in Fig. 13. In FGM 5, due to the combination of different compositional regions, at 5% elongation, the maximum strain was observed in a region containing about 65 wt.% of stainless steel. It is perceived that with stainless steel being softer in this region, the deformation will start at this region, and then at around 15% of deformation, the load starts to be transferred to Inconel. Failure occurred in FGM 5 at around 65 wt.% of stainless steel. The presence of MC carbides and δ-phase (Ni_3Nb) in an austenitic matrix may be responsible for the location of the failure. It must be noted that in every specimen of this condition, failure occurred in this region.

Concerning the specimens taken from samples FGM 100-100, fracture always occurred in the direct interface between the two materials with elongations up to 65%. Until an elongation of 20% deformation, deformation remained almost symmetrical in both as-built materials. At 40%, deformation started to increase near the interface, then failure occurred.

Fractography of the FGM 100-100 (Fig. 14a) samples had a ductile aspect with a fracture surface mainly composed of homogeneously distributed fine dimples, which correlates well with the high elongation at fracture exhibited in this sample. The fracture surface of the FGM 5 samples (Fig. 14b) indicates a mixture of fracture aspects, with dimples and quasi-cleavage facets. Despite this, the FGM 5 sample still had a high elongation at fracture. This quasi-cleavage aspect was attributed to the presence of TCP phases in this region [20]. The fractography of both control samples (stainless steel 316 and Inconel 625) showed a ductile-like aspect composed mainly of large and homogenously dispersed dimples.

4. Conclusions

The present work attempts to optimize and compare properties of FGMs based on 316L stainless and Inconel 625 built with different deposition strategies (direct and smooth-type interfaces). At the interface of the smooth transition FGM, secondary phases that were not present in the as-built materials, such as the δ-phase (Ni_3Nb) and MC carbides, were detected by synchrotron X-ray diffraction. However, none of these phases were formed when using a direct interface. The FGMs built with a direct interface (FGM 100-100) showed, on average, a strength of 542 MPa and elongation up to 61.6%. The smooth transition FGM (FGM 5) had a lower strength of 503 MPa and elongation of 32.4%. The fracture location in the direct and smooth-type transition was located at the 50 and 65 wt.% of stainless-steel regions, respectively. The specimens underwent a predominantly ductile-like fracture with considerable plastic deformation in all the tensile tests. The residual stresses measurements, as determined by neutron diffraction, showed stresses in the interface of the FGM 100-100 only up to a magnitude up to 180 MPa, while the FGM 5 experienced stresses up to 314, 348, and 468 MPa in the x, y, and z directions, respectively.

Data availability

The raw/processed data required to reproduce these findings cannot be shared at this time as the data also forms part of an ongoing study.

Declaration of Competing Interest

The authors declare that they have no known competing financial interests or personal relationships that could have appeared to influence the work reported in this paper.

Acknowledgments

TAR acknowledges FCT–MCTES for funding the Ph.D. grant SFRH/BD/144202/2019. TAR, AM, FF, TGS, and JPO acknowledge Fundação para a Ciência e a Tecnologia (FCT–MCTES) for its financial support via the project UID/00667/2020 (UNIDEMI). JPO acknowledges the funding of CENIMAT/i3N by national funds through the FCT-Fundação para a Ciência e a Tecnologia, IP, within the scope of Multiannual Financing of R&D Units, reference UIDB/50025/2020-2023. JS acknowledges the China Scholarship Council for funding the Ph.D. grant (CSC NO. 201808320394). This activity has received funding from the European Institute of Innovation and Technology (EIT) – Project Smart WAAM: Microstructural Engineering and Integrated Non-Destructive Testing. This body of the European Union receives support from the European Union's Horizon 2020 research and innovation program. The authors acknowledge DESY (Hamburg, Germany), a member of the Helmholtz Association HGF, for providing experimental facilities. Beamtime was allocated for proposal I-20210899 EC. The research leading to this result has been supported by the project CALIPSOplus under the Grant Agreement 730872 from the EU Framework Programme for Research and Innovation HORIZON 2020.

REFERENCES

[1] Wang SS. Fracture mechanics for delamination problems in composite materials. In: Studies in Applied Mathematics. Elsevier Science Publishers B.V.; 1984. p. 369–83. https://doi.org/10.1016/B978-0-444-42169-2.50029-2.

[2] Zhang C, Chen F, Huang Z, Jia M, Chen G, Ye Y, et al. Additive manufacturing of functionally graded materials: a review. Mater Sci Eng A 2019;764:138209. https://doi.org/10.1016/j.msea.2019.138209.

[3] Pietrzak K, Kaliński D, Chmielewski M. Interlayer of Al2O3–Cr functionally graded material for reduction of thermal stresses in alumina–heat resisting steel joints. J Eur Ceram Soc 2007;27:1281–6. https://doi.org/10.1016/j.jeurceramsoc.2006.04.102.

[4] Wu D, Shi J, Niu F, Ma G, Zhou C, Zhang B. Direct additive manufacturing of melt growth Al2O3-ZrO2 functionally graded ceramics by laser directed energy deposition. J Eur Ceram Soc 2022;42:2957–73. https://doi.org/10.1016/j.jeurceramsoc.2022.01.034.

[5] Carroll BE, Palmer TA, Beese AM. Anisotropic tensile behavior of Ti–6Al–4V components fabricated with directed energy deposition additive manufacturing. Acta Mater 2015;87:309–20. https://doi.org/10.1016/j.actamat.2014.12.054.

[6] Varghese P, Vetrivendan E, Dash MK, Ningshen S, Kamaraj M, Kamachi Mudali U. Weld overlay coating of Inconel 617 M on type 316 L stainless steel by cold metal transfer process. Surf Coat Technol 2019;357:1004–13. https://doi.org/10.1016/j.surfcoat.2018.10.073.

[7] Bloemer PRA, Pacheco JT, Cunha A, Veiga MT, Filho OCM, Meura VH, et al. Laser cladding of inconel 625 on AISI 316L: microstructural and mechanical evaluation of parameters estimated by empirical-statistical model. J Mater Eng Perform 2022;31:211–20. https://doi.org/10.1007/s11665-021-06147-8.

[8] Farias FWC, Payão Filho JC, da Silva Júnior DA, de Moura RN, Rios MCG. Microstructural characterization of Ni-based superalloy 625 clad welded on a 9% Ni steel pipe by plasma powder transferred arc. Surf Coat Technol 2019;374:1024–37. https://doi.org/10.1016/j.surfcoat.2019.06.084.

[9] Shah K, ul Haq I, Khan A, Shah SA, Khan M, Pinkerton AJ. Parametric study of development of Inconel-steel functionally graded materials by laser direct metal deposition. Mater Des 2014;54:531–8. https://doi.org/10.1016/j.matdes.2013.08.079.

[10] Kou S. Solidification and liquation cracking issues in welding. JOM 2003;55:37–42. https://doi.org/10.1007/s11837-003-0137-4.

[11] Chen N, Khan HA, Wan Z, Lippert J, Sun H, Shang S-L, et al. Microstructural characteristics and crack formation in additively manufactured bimetal material of 316L stainless steel and Inconel 625. Addit Manuf 2020;32:101037. https://doi.org/10.1016/j.addma.2020.101037.

[12] Carroll BE, Otis RA, Borgonia JP, Suh JO, Dillon RP, Shapiro AA, et al. Functionally graded material of 304L stainless steel and inconel 625 fabricated by directed energy deposition: characterization and thermodynamic modeling. Acta Mater 2016;108:46–54. https://doi.org/10.1016/j.actamat.2016.02.019.

[13] Rodrigues TA, Bairrão N, Farias FWC, Shamsolhodaei A, Shen J, Zhou N, et al. Steel-copper functionally graded material produced by twin-wire and arc additive manufacturing (T-WAAM). Mater Des 2022;213:110270. https://doi.org/10.1016/j.matdes.2021.110270.

[14] Hammersley AP, Svensson SO, Hanfland M, Fitch AN, Hausermann D. Two-dimensional detector software: from real detector to idealised image or two-theta scan. High Pres Res 1996;14:235–48. https://doi.org/10.1080/08957959608201408.

[15] Arnold O, Bilheux JC, Borreguero JM, Buts A, Campbell SI, Chapon L, et al. Mantid—data analysis and visualization package for neutron scattering and μ SR experiments. Nucl Instruments Methods Phys Res Sect A Accel Spectrometers Detect Assoc Equip 2014;764:156–66. https://doi.org/10.1016/j.nima.2014.07.029.

[16] Sorger GL, Oliveira JP, Inácio PL, Enzinger N, Vilaça P, Miranda RM, et al. Non-destructive microstructural analysis by electrical conductivity: comparison with hardness measurements in different materials. J Mater Sci Technol 2019;35:360–8. https://doi.org/10.1016/j.jmst.2018.09.047.

[17] Blaber J, Adair B, Antoniou A. Ncorr: open-source 2D digital image correlation matlab software. Exp Mech 2015;55:1105–22. https://doi.org/10.1007/s11340-015-0009-1.

[18] Elmer JW, Allen SM, Eagar TW. Microstructural development during solidification of stainless steel alloys. Metall Trans A 1989;20:2117–31. https://doi.org/10.1007/BF02650298.

[19] Silva CC, de Albuquerque VHC, Miná EM, Moura EP, Tavares JMRS. Mechanical properties and microstructural characterization of aged nickel-based alloy 625 weld metal. Metall Mater Trans A Phys Metall Mater Sci 2018;49:1653–73. https://doi.org/10.1007/s11661-018-4526-2.

[20] Sui S, Tan H, Chen J, Zhong C, Li Z, Fan W, et al. The influence of Laves phases on the room temperature tensile properties of Inconel 718 fabricated by powder feeding laser additive

manufacturing. Acta Mater 2019;164:413–27. https://doi.org/10.1016/j.actamat.2018.10.032.
[21] Landowski M, Świerczyńska A, Rogalski G, Fydrych D. Autogenous fiber laser welding of 316L austenitic and 2304 lean duplex stainless steels. Materials 2020;13:2930. https://doi.org/10.3390/ma13132930.
[22] Silva CC, de Albuquerque VHC, Miná EM, Moura EP, Tavares JMRS. Mechanical properties and microstructural characterization of aged nickel-based alloy 625 weld metal. Metall Mater Trans 2018;49:1653–73. https://doi.org/10.1007/s11661-018-4526-2.
[23] Cieslak MJ, Headley TJ, Romig AD, Kollie T. A melting and solidification study of alloy 625. Metall Trans A 1988;19:2319–31. https://doi.org/10.1007/BF02645056.
[24] Cao W-D, Kennedy R. Role of chemistry in 718-type Alloys: Allvac 718plus alloy development. Tenth Int. Symp., TMS. In: Superalloys 2004; 2004. p. 91–9. https://doi.org/10.7449/2004/Superalloys_2004_91_99.
[25] Kou S. A criterion for cracking during solidification. Acta Mater 2015;88:366–74. https://doi.org/10.1016/j.actamat.2015.01.034.
[26] Liu J, Kou S. Effect of diffusion on susceptibility to cracking during solidification. Acta Mater 2015;100:359–68. https://doi.org/10.1016/j.actamat.2015.08.064.
[27] Soysal T, Kou S, Tat D, Pasang T. Macrosegregation in dissimilar-metal fusion welding. Acta Mater 2016;110:149–60. https://doi.org/10.1016/j.actamat.2016.03.004.
[28] Hofmann DC, Kolodziejska J, Roberts S, Otis R, Dillon RP, Suh J-O, et al. Compositionally graded metals: a new frontier of additive manufacturing. J Mater Res 2014;29:1899–910. https://doi.org/10.1557/jmr.2014.208.
[29] Rodrigues TA, Duarte V, Avila JA, Santos TG, Miranda RM, Oliveira JP. Wire and arc additive manufacturing of HSLA steel: effect of thermal cycles on microstructure and mechanical properties. Addit Manuf 2019;27:440–50. https://doi.org/10.1016/j.addma.2019.03.029.
[30] Farias FWC, da Cruz Payão Filho J, Moraes e Oliveira VHP. Prediction of the interpass temperature of a wire arc additive manufactured wall: FEM simulations and artificial neural network. Addit Manuf 2021;48:102387. https://doi.org/10.1016/j.addma.2021.102387.
[31] Chandra K, Kumar NN, Kain V. Effect of retained δ-ferrite transforming to sigma phase on the hardness and corrosion resistance of stainless steel 321. Trans Indian Inst Met 2022;75:959–66. https://doi.org/10.1007/s12666-022-02534-4.
[32] Ramkumar KD, Varma JLN, Chaitanya G, Choudhary A, Arivazhagan N, Narayanan S. Effect of autogeneous GTA welding with and without flux addition on the microstructure and mechanical properties of AISI 904L joints. Mater Sci Eng A 2015;636:1–9. https://doi.org/10.1016/j.msea.2015.03.072.
[33] Kim SH, Lee H, Yeon SM, Aranas C, Choi K, Yoon J, et al. Selective compositional range exclusion via directed energy deposition to produce a defect-free Inconel 718/SS 316L functionally graded material. Addit Manuf 2021;47:102288. https://doi.org/10.1016/j.addma.2021.102288.
[34] Yang SW, Yoon J, Lee H, Shim DS. Defect of functionally graded material of inconel 718 and STS 316L fabricated by directed energy deposition and its effect on mechanical properties. J Mater Res Technol 2022;17:478–97. https://doi.org/10.1016/j.jmrt.2022.01.029.